



# Non-Hermitian higher-order topological superconductors in two-dimension: statics and dynamics

Arnob Kumar Ghosh <sup>1,2,\*</sup> and Tanay Nag <sup>3,†</sup>

<sup>1</sup>*Institute of Physics, Sachivalaya Marg, Bhubaneswar-751005, India*

<sup>2</sup>*Homi Bhabha National Institute, Training School Complex, Anushakti Nagar, Mumbai 400094, India*

<sup>3</sup>*Department of Physics and Astronomy, Uppsala University, Box 516, 75120 Uppsala, Sweden*

Being motivated by intriguing phenomena such as the breakdown of conventional bulk boundary correspondence and emergence of skin modes in the context of non-Hermitian (NH) topological insulators, we here propose a NH second-order topological superconductor (SOTSC) model that hosts Majorana zero modes (MZMs). Employing the non-Bloch form of NH Hamiltonian, we topologically characterize the above modes by biorthogonal nested polarization and resolve the apparent breakdown of the bulk boundary correspondence. Unlike the Hermitian SOTSC, we notice that the MZMs inhabit only one corner out of four in the two-dimensional NH SOTSC. Such localization profile of MZMs is protected by mirror rotation symmetry and remains robust under on-site random disorder. We extend the static MZMs into the realm of Floquet drive. We find anomalous  $\pi$ -mode following low-frequency mass-kick in addition to the regular 0-mode that is usually engineered in a high-frequency regime. We further characterize the regular 0-mode with biorthogonal Floquet nested polarization. Our proposal is not limited to the  $d$ -wave superconductivity only and can be realized in the experiment with strongly correlated optical lattice platforms.

**Introduction.**— In recent times, topological phases in insulators and superconductors are extensively studied theoretically [1–6] as well as experimentally [7, 8]. The conventional bulk boundary correspondence (BBC) for first-order topological phase is generalized for  $n(>1)$ th-order topological insulator (TI) [9–20] and topological superconductor [21–41] in  $d \geq 2$  dimensions where there exist  $n_c = (d - n)$ -dimensional boundary modes. The zero-dimensional (0D) corner and one-dimensional (1D) hinge modes are thus the hallmark signatures of higher-order topological insulator (HOTI) and higher-order topological superconductor (HOTSC). The dynamic analog of these phases are extensively studied for Floquet HOTI (FHOTI) [42–59] and Floquet HOTSC (FHOTSC) [60–66].

The realm of topological quantum matter is transcended from the Hermitian system to the non-Hermitian (NH) system due to the practical realization of TI phases in meta-materials [67–70] where energy conservation no longer holds [71, 72]. The NH description has a wide range of applications, including systems with source and drain [73, 74], in contact with the environment [75–77], and involving quasiparticles of finite lifetime [78–80]. Apart from the complex eigenenergies and non-orthogonal eigenstates, the NH Hamiltonians uncover a plethora of intriguing phenomena in TI [72, 81–84] that do not have any Hermitian analog. For instance, NH Hamiltonian becomes non-diagonalizable at exceptional points (EPs) where eigenstates, corresponding to degenerate bands, coalesce [85, 86]; line and point are two different types of gaps in these systems that can be adiabatically transformed into a Hermitian and NH systems,

respectively [82]; the conventional Bloch wave functions do not precisely indicate the topological phase transitions under the open-boundary conditions (OBCs) leading to the breakdown of the BBC [87–93]; consequently, the non-Bloch-wave behavior results in the skin effect where the bulk states accumulate at the boundary [87–89, 94], and the structure of topological invariants become intricate [81, 95–97]. The EPs are studied in the context of Floquet NH Weyl semimetals [98, 99].

While much has been explored on the HOTI phases in the context of NH systems [100–109], HOTSC counterpart, along with its dynamic signature, is yet to be examined. Note that NH 1D nanowire with  $s$ -wave pairing and  $p$ -wave SC chain are studied for the Majorana zero modes (MZMs) [110–116]. We, therefore, seek the answers to the following questions that have not been addressed so far in the context of proximity induced HOTSC with non-hermiticity -(a) How does the BBC change as compared to the Hermitian case? (b) Can one use the concept of biorthogonal nested-Wilson-loop to characterize the MZMs there similar to that for HOT electronic modes [101]? (c) How can one engineer the anomalous FHOTSC phase for the NH case?

Considering the NH TI in the proximity to a  $d$ -wave superconductor, we illustrate the generation of the NH second-order topological superconductor (SOTSC). The breakdown of BBC is resolved with the non-Bloch nature of the NH Hamiltonian, where phase boundaries, obtained under different boundary conditions, become concurrent with each other (see Fig. 1). The SOTSC phase is characterized by the non-Bloch nested polarization. We demonstrate the NH skin effect where MZMs and bulk modes both display substantial corner localization (see Fig. 2). We further engineer the regular 0- and anomalous  $\pi$ -mode employing the mass-drive in high- and low-frequency regimes, respectively (see Figs. 3 and 4). We characterize the regular dynamic 0-mode by the

\* arnob@iopb.res.in

† tanay.nag@physics.uu.se

non-Bloch Floquet nested polarization.

**Realization of NH SOTSC.**— We contemplate the following Hamiltonian of the NH SOTSC, consisting of NH TI  $H_{\text{TI}}(\mathbf{k})$  and  $d$ -wave proximitized superconductivity [23, 64]

$$\mathcal{H}(\mathbf{k}) = \begin{pmatrix} H_{\text{TI}}(\mathbf{k}) - \mu & \Delta \\ \Delta^* & \mu - \tilde{H}_{\text{TI}}(-\mathbf{k}) \end{pmatrix}, \quad (1)$$

where,  $\tilde{H}_{\text{TI}}(\mathbf{k}) = U_{\mathcal{T}}^{-1} H_{\text{TI}}^*(\mathbf{k}) U_{\mathcal{T}}$ . Here,  $H_{\text{TI}}(\mathbf{k}) = (\lambda_x \sin k_x + i\gamma_x)\sigma_x s_z + (\lambda_y \sin k_y + i\gamma_y)\sigma_y s_0 + (m_0 - t_x \cos k_x - t_y \cos k_y)\sigma_z s_0 = H_{\text{TI}}^{\text{H}}(\mathbf{k}) + i\gamma_x \sigma_x s_z + i\gamma_y \sigma_y s_0$ , that preserves ramified (time-reversal symmetry) TRS:  $U_{\mathcal{T}} \mathcal{H}_{\text{TI}}^*(\mathbf{k}) U_{\mathcal{T}}^{-1} = \mathcal{H}_{\text{TI}}(-\mathbf{k})$  and (particle-hole symmetry) PHS $^\dagger$ :  $U_{\mathcal{C}} \mathcal{H}_{\text{TI}}^*(\mathbf{k}) U_{\mathcal{C}}^{-1} = -\mathcal{H}_{\text{TI}}(-\mathbf{k})$  with  $U_{\mathcal{T}} = \sigma_0 s_y$  and  $U_{\mathcal{C}} = \sigma_x s_0$ , respectively [82]. The  $d$ -wave superconducting pairing is given by  $\Delta(\mathbf{k}) = \Delta(\cos k_x - \cos k_y)$ ; whereas  $\gamma_x$  and  $\gamma_y$  introduce non-hermiticity in the Hamiltonian such that  $H_{\text{TI}}(\mathbf{k}) \neq H_{\text{TI}}^\dagger(\mathbf{k})$ . The hopping (spin-orbit coupling) amplitudes are given by  $t_{x,y}$  ( $\lambda_{x,y}$ ). Here,  $m_0$  and  $\mu$  account for the crystal field splitting and chemical potential, respectively. Notice that,  $H_{\text{TI}}^{\text{H}}(\mathbf{k})$  respects TRS:  $\mathcal{T} H_{\text{TI}}^{\text{H}}(\mathbf{k}) \mathcal{T}^{-1} = H_{\text{TI}}^{\text{H}}(-\mathbf{k})$  and PHS:  $\mathcal{C} H_{\text{TI}}^{\text{H}}(\mathbf{k}) \mathcal{C}^{-1} = -H_{\text{TI}}^{\text{H}}(-\mathbf{k})$ ; with  $\mathcal{T} = iU_{\mathcal{T}}\mathcal{K}$  and  $\mathcal{C} = U_{\mathcal{C}}\mathcal{K}$ . The Hamiltonian (S1) thus takes the following compact form  $\mathcal{H}(\mathbf{k}) = \mathbf{N} \cdot \mathbf{\Gamma}$ ; where,  $\mathbf{N} = \{\lambda_x \sin k_x + i\gamma_x, \lambda_y \sin k_y + i\gamma_y, m_0 - t_x \cos k_x - t_y \cos k_y, \Delta(\mathbf{k})\}$ ,  $\mathbf{\Gamma} = \{\tau_z \sigma_x s_z, \tau_z \sigma_y s_0, \tau_z \sigma_z s_0, \tau_x \sigma_0 s_0\}$  with the Pauli matrices  $\boldsymbol{\tau}$ ,  $\boldsymbol{\sigma}$ , and  $s$  act on PH ( $e, h$ ), orbital ( $\alpha, \beta$ ), and spin ( $\uparrow, \downarrow$ ) degrees of freedom, respectively. Note that,  $\mathcal{H}(\mathbf{k})$  obeys TRS and PHS $^\dagger$ , generated by  $\tilde{U}_{\mathcal{T}} = \tau_0 \sigma_0 s_y$  and  $\tilde{U}_{\mathcal{C}} = \tau_y \sigma_0 s_y$ , respectively. In addition,  $\mathcal{H}(\mathbf{k})$  preserves sublattice/ chiral symmetry  $\mathcal{S} = \tau_y \sigma_0 s_0$  such that  $\mathcal{S} \mathcal{H}(\mathbf{k}) \mathcal{S}^{-1} = -\mathcal{H}(\mathbf{k})$ . Now coming to the crystalline symmetries of the model with  $t_x = t_y$ ,  $\lambda_x = \lambda_y$ , and  $|\gamma_x| = |\gamma_y| \neq 0$ , we find that  $\mathcal{H}(\mathbf{k})$  breaks four-fold rotation with respect to  $z$ ,  $C_4 = \tau_z e^{-i\frac{\pi}{4}\sigma_z s_z}$ , mirror-reflection along  $x$ ,  $\mathcal{M}_x = \tau_x \sigma_x s_0$  and mirror-reflection along  $y$ ,  $\mathcal{M}_y = \tau_x \sigma_y s_0$ . As a result,  $\mathcal{H}(\mathbf{k})$  preserves mirror-rotation I  $\mathcal{M}_{xy} = C_4 \mathcal{M}_y$  for  $\gamma_x = \gamma_y \neq 0$ , and mirror-rotation II  $\mathcal{M}_{x\bar{y}} = C_4 \mathcal{M}_x$  for  $\pm\gamma_x = \mp\gamma_y \neq 0$ , such that  $\mathcal{M}_{xy} \mathcal{H}(k_x, k_y) \mathcal{M}_{xy}^{-1} = \mathcal{H}(k_y, k_x)$  and  $\mathcal{M}_{x\bar{y}} \mathcal{H}(k_x, k_y) \mathcal{M}_{x\bar{y}}^{-1} = \mathcal{H}(-k_y, -k_x)$ , respectively (see supplemental material [117]).

We note at the outset that the definition of Majorana for NH system is different from its Hermitian analogue. The PHS $^\dagger$  in NH case allows us to define a modified Hermitian conjugate operation such that MZMs obey an effective Hermiticity  $\Gamma_n^a = c_n + \bar{c}_n$ ,  $\Gamma_n^b = i(c_n - \bar{c}_n)$ , and  $\bar{\Gamma}_n^{a,b} = \Gamma_n^{a,b}$  [110]; ( $\bar{c}_n, c_n$ ) denote the creation and annihilation operators of the Bogoliubov quasi-particles where  $\bar{c}_n$  does not correspond to Hermitian conjugate of  $c_n$  in presence of non-Hermiticity. However, the extraction of real MZMs individually remains unaddressed out of more than two Majorana corner modes.

The Hermitian system  $\mathcal{H}^{\text{H}}(\mathbf{k})$  hosts zero-energy Majorana corner modes, protected by the TRS, in SOTSC phase for  $m_0 < |t_x + t_y|$  while trivially gapped for  $m_0 > |t_x + t_y|$  [23]. The NH system becomes defective at EPs

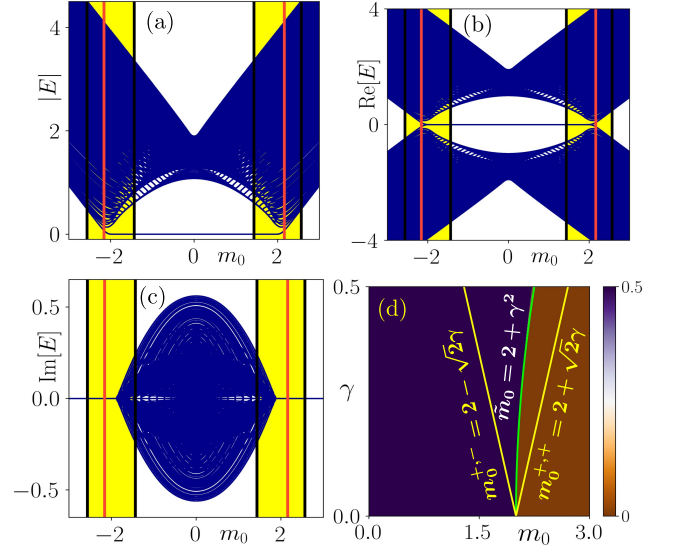


FIG. 1. We show  $|E|$ ,  $\text{Re}[E]$ , and  $\text{Im}[E]$ , obtained from real space Hamiltonian under OBC in all directions using Eq. (S1), as a function of  $m_0$  in (a), (b), and (c), respectively. The mid-gap MZMs disappear into the bulk bands at  $m_0 = \tilde{m}_0 = \pm(t_x + t_y + \gamma_x^2/2\lambda_x^2 + \gamma_y^2/2\lambda_y^2)$ , defined by the red lines. The EPs  $m_0^{s,\pm} = s(t_x + t_y) \pm \sqrt{\gamma_x^2 + \gamma_y^2}$  with  $s = \pm$  are marked by black lines within which  $\text{Re}[E(k)]$  associated with  $\mathcal{H}(\mathbf{k})$  remains gapless as designated by yellow-shaded region. (d) The topological phase diagram is depicted in the  $m_0$ - $\gamma$  plane using nested polarization  $\langle \nu_{y,\mu}^{\nu_x} \rangle$  Eq. (7). The yellow and green lines correspond to  $m_0^{+,\pm}$  and  $\tilde{m}_0$ , respectively while the later separates SOTSC phase  $\langle \nu_{y,\mu}^{\nu_x} \rangle = 0.5$  from the trivial phase  $\langle \nu_{y,\mu}^{\nu_x} \rangle = 0.0$ . The parameters used here are  $t_x = t_y = \lambda_x = \lambda_y = \Delta = 1.0$  and  $\gamma_x = \gamma_y = 0.4$ .

provided  $|E(\mathbf{k}_{\text{EP}})| = 0$  which is in a complete contrast to the Hermitian system with  $E(\mathbf{k}) = 0$  at gapless point. A close inspection of Eq. (S1) suggests that four-fold degenerate energy bands yield  $|E(0,0)| = 0$  [ $|E(\pi,\pi)| = 0$ ] for  $m_0^{+,\pm} = t_x + t_y \pm \sqrt{\gamma_x^2 + \gamma_y^2}$  [ $m_0^{-,\pm} = -t_x - t_y \pm \sqrt{\gamma_x^2 + \gamma_y^2}$ ]. As a result, the gapless phase boundaries  $m_0^s = s(t_x + t_y)$  for the Hermitian case are modified in the present NH case with  $m_0^{s,\pm} = s(t_x + t_y) \pm \sqrt{\gamma_x^2 + \gamma_y^2}$ , where,  $s = \pm$  (see black lines in Figs. 1 (a)-(c)). This refers to the fact that  $\text{Re}[E(\mathbf{k})]$  is gapless for  $m_0^{\pm,-} < m_0 < m_0^{\pm,+}$  (see yellow-shaded region in Figs. 1 (a)-(c)). Furthermore,  $\mathcal{H}(\mathbf{k})$  is expected to be gapped in real sector of energy for  $m_0^{-,+} < m_0 < m_0^{+,-}$ , hosting NH SOTSC phase.

The above conjecture, based on periodic boundary condition (PBC), is drastically modified when the NH system (S1) is investigated under OBC. We show  $|E|$ ,  $\text{Re}[E]$  and  $\text{Im}[E]$  under OBC with blue points in Figs. 1 (a), (b), and (c), respectively. Surprisingly, the MZMs continue to survive inside the yellow-shaded region i.e., beyond  $m_0 = m_0^{+,-}$  and  $m_0 = m_0^{-,+}$ , till  $m_0 < |\tilde{m}_0| = t_x + t_y + \gamma_x^2/2\lambda_x^2 + \gamma_y^2/2\lambda_y^2$ , depicted by the red line, where the  $\text{Re}[E]$  becomes gapless. All together this suggests the

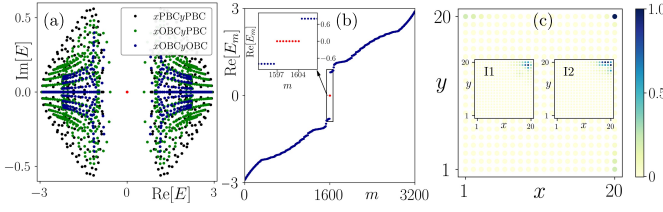


FIG. 2. (a) The eigenvalue spectrum for the real space 2D system Eq. (S1), obeying PBC in both direction (black dots), PBC in  $y$  and OBC in  $x$ -direction (green dots), and OBC in both directions (blue dots) are depicted in complex energy plane. The zero-energy mode, obtained from OBC, is marked by red dots. (b)  $\text{Re}[E_m]$  as a function of the state index  $m$  is displayed where eight mid-gap MZMs are highlighted in the inset. (c) The LDOS, associated with eight MZMs in (b), show sharp localization only at one corner. The LDOS for typical bulk states are shown in insets I1 (for  $E_m = -2.631839$ ) and I2 (for  $E_m = -1.738466 + 0.130006i$ ). We use  $m_0 = 1.0$ , while other parameters are same as Fig. 1.

break-down of conventional BBC due to the non-Bloch nature of the NH Hamiltonian [87, 91–93]. This apparent ambiguity in BBC affects the calculation of topological invariants, which we investigate below.

Fig. 2 (a) demonstrates the complex-energy profile  $\text{Im}[E]$  vs  $\text{Re}[E]$  of Hamiltonian (S1) in real space for  $m_0 < |\tilde{m}_0|$ . We find the line gap for the NH system irrespective of the boundary conditions as the complex-energy bands do not cross a reference line in the complex-energy plane. The origin, marked with red dot in Fig. 2 (a), indicates the MZMs under OBC that are further shown by the eight mid-gap states in  $\text{Re}[E]-m$  (state index) plot (see Fig. 2 (b)). Analyzing the local density of states (LDOS) of the above MZMs, we find sharp localization only at one corner out of the four corners [100] (see Fig. 2 (c)). This is a consequence of the mirror-rotation symmetries  $\mathcal{M}_{xy}$  or  $\mathcal{M}_{x\bar{y}}$  even though MZMs spatially coincide. There might be additional protection from the bulk modes coming due to the emergent short-range nature of the superconducting gap [118]. The MZMs are localized over more than a single corner when  $\mathcal{M}_{xy}$  or  $\mathcal{M}_{x\bar{y}}$  is broken [117]. The MZMs are also found to be robust against onsite disorder that respects mirror-rotation and chiral symmetries (see supplemental material [117]). In addition, we remarkably find that the LDOS of the bulk modes also exhibits substantial corner localization as depicted in the insets of Fig. 2(c) [87–89]. The above features, reflecting the non-Block nature of the system, are referred to as the NH skin effect [87, 88]. This is in contrast to the Hermitian case where only the zero-energy modes can populate four corners of the 2D square lattice [13, 43, 47].

**Topological characterization.**— To this end, in order to compute the topological invariant from  $\mathcal{H}(\mathbf{k})$  characterizing the SOTSC phase under OBC, we exploit the non-Bloch nature. We need to use the complex wave-vectors to describe open-boundary eigenstates such that

$\mathbf{k} \rightarrow \mathbf{k}' + i\beta$  with  $\beta_i = \gamma_i/\lambda_i$  ( $i = x, y$ ) [81]. Upon replacing  $k_{x,y} \rightarrow k'_{x,y} - i\gamma_{x,y}/\lambda_{x,y}$ , the renormalized topological mass  $m'_0$  acquires the following form in the limit  $k_{x,y} \rightarrow 0$  and  $\gamma_{x,y} \rightarrow 0$

$$m'_0 = m_0 - t_x - t_y - \frac{\gamma_x^2}{2\lambda_x^2} - \frac{\gamma_y^2}{2\lambda_y^2}. \quad (2)$$

Note that  $|\tilde{m}_0| = |m'_0 - m_0|$  denotes phase boundary of the SOTSC phase as obtained from Fig. 1 (b). Employing  $\mathbf{k}' \rightarrow \mathbf{k}'$  in  $\mathcal{H}(\mathbf{k})$  i.e.,  $\mathcal{H}(\mathbf{k}) \rightarrow \mathcal{H}'(\mathbf{k}')$ , we construct the Wilson loop operator as [10, 66]

$$W_{x,\mathbf{k}'} = F_{x,\mathbf{k}'+(L_x-1)\Delta_x\mathbf{e}_x}(t) \cdots F_{x,\mathbf{k}'+\Delta_x\mathbf{e}_x} F_{x,\mathbf{k}'} \quad (3)$$

from the non-Bloch NH Hamiltonian  $\mathcal{H}'(\mathbf{k}')$  [119, 120]. We define  $[F_{x,\mathbf{k}'}]_{mn} = \langle \Psi_m^L(\mathbf{k}' + \Delta_x\mathbf{e}_x) | \Psi_n^R(\mathbf{k}') \rangle$ , where  $|\Psi_m^R(\mathbf{k}')\rangle$  ( $\langle \Psi_m^L(\mathbf{k}')|$ ) represents the occupied right (left) eigenvectors of the Hamiltonian  $\mathcal{H}'(\mathbf{k}')$  such that  $\text{Re}[E_m(\mathbf{k}')] < 0$ ;  $\Delta_i = 2\pi/L_i$ , with  $L_i$  being the number of discrete points considered along  $i$ -th direction and  $\mathbf{e}_i$  being the unit vector along the said direction. Notice that, the bi-orthogonalization guarantees the following  $\sum_n |\Psi_n^R(\mathbf{k}')\rangle \langle \Psi_n^L(\mathbf{k}')| = \mathbb{I}$  and  $\langle \Psi_n^L(\mathbf{k}') | \Psi_n^R(\mathbf{k}') \rangle = \delta_{mn}$ ; where,  $n$  runs over all the energy levels irrespective of their occupations. The first-order polarization  $\nu_{x,\mu}(k'_y)$  is obtained from the eigenvalue equation for  $W_{x,\mathbf{k}'}$  as follows

$$W_{x,\mathbf{k}'} |\nu_{x,\mu}^R(\mathbf{k}')\rangle = e^{-2\pi i \nu_{x,\mu}(k'_y)} |\nu_{x,\mu}^R(\mathbf{k}')\rangle. \quad (4)$$

Note that unlike the Hermitian case, here  $W_{x,\mathbf{k}'}$  is no longer unitary resulting in  $\nu_{x,\mu}(k'_y)$  to be a complex number [101]. Importantly,  $|\nu_{x,\mu}^R(\mathbf{k}')\rangle$  ( $\langle \nu_{x,\mu}^L(\mathbf{k}')|$ ) designates bi-orthogonalized right (left) eigenvector of  $W_{x,\mathbf{k}'}$  associated with  $\mu = 1, \dots, 4$ -th eigenvalue. For a (second-order topological) SOT system, the real part of first-order polarization exhibits a finite gap in spectra such that it can be divided into two sectors as  $\pm \nu_x(k'_y)$  where each sector is two-fold degenerate. Such a structure of Wannier centres in the non-Bloch case might be relied on the mirror symmetry of the underlying Hermitian Hamiltonian [10, 66]. In order to characterize the SOT phase, we calculate the polarization along the perpendicular  $y$ -direction by projecting onto each  $\pm \nu_x$  branch. This allows us to employ the nested Wilson loop as follows [10, 66]

$$W_{y,\mathbf{k}'}^{\pm \nu_x} = F_{y,\mathbf{k}'+(L_y-1)\Delta_y\mathbf{e}_y}^{\pm \nu_x} \cdots F_{y,\mathbf{k}'+\Delta_y\mathbf{e}_y}^{\pm \nu_x} F_{y,\mathbf{k}'}^{\pm \nu_x}. \quad (5)$$

Here,  $[F_{y,\mathbf{k}'}^{\pm \nu_x}]_{\mu_1\mu_2} = \sum_{mn} [\nu_{x,\mu_1}^L(\mathbf{k}' + \Delta_y\mathbf{e}_y)]_m^* [F_{y,\mathbf{k}'}]_{mn} [\nu_{x,\mu_2}^R(\mathbf{k}')]_n$  with  $[F_{y,\mathbf{k}'}]_{mn} = \langle \Psi_m^L(\mathbf{k}' + \Delta_y\mathbf{e}_y) | \Psi_n^R(\mathbf{k}') \rangle$ . The indices  $\mu_{1,2} \in \pm \nu_x$  run over the projected eigenvectors of  $W_{x,\mathbf{k}'}$  only. We evaluate  $W_{y,\mathbf{k}'}^{\pm \nu_x}$  for a given value of  $k'_x$  that is the base point while calculating  $W_{x,\mathbf{k}'}$  (3).

The nested polarization  $\nu_{y,\mu'}^{\pm \nu_x}(k'_x)$  can be extracted by solving the eigenvalue equation for  $W_{y,\mathbf{k}'}^{\pm \nu_x}$

$$W_{y,\mathbf{k}'}^{\pm \nu_x} |\nu_{y,\mu'}^{\pm \nu_x}(\mathbf{k}')\rangle = e^{-2\pi i \nu_{y,\mu'}^{\pm \nu_x}(k'_x)} |\nu_{y,\mu'}^{\pm \nu_x}(\mathbf{k}')\rangle. \quad (6)$$

The average nested Wannier sector polarization  $\langle \nu_{y,\mu'}^{\pm\nu_x} \rangle$  for the  $\mu'$ -th branch, characterizing the 2D SOTSC, is given by

$$\langle \nu_{y,\mu'}^{\pm\nu_x} \rangle = \frac{1}{L_x} \sum_{k'_x} \text{Re} \left[ \nu_{y,\mu'}^{\pm\nu_x}(k'_x) \right]. \quad (7)$$

We explore the SOT phase diagram by investigating  $\text{mod}(\langle \nu_{y,\mu'}^{\pm\nu_x} \rangle, 1.0)$  in the  $m_0$ - $\gamma$  ( $\gamma_x = \gamma_y = \gamma$ ) plane keeping  $t_x = t_y = \lambda_x = \lambda_y = 1$  (see Fig. 1(d)). The blue (brown) region indicates the SOTSC and trivial phase. The green line in Fig. 1 (d), separating the above two phases, represents the phase boundary  $\tilde{m}_0 = 2 + \gamma^2$  as demonstrated in Eq. (2). On the other hand, the phase boundaries, obtained from bulk Hamiltonian (S1), are found to be  $m_0^{\pm} = 2 \pm \sqrt{2}\gamma$  that are depicted by yellow lines in Fig. 1 (d). Therefore, the topological invariant, computed using the non-Bloch Hamiltonian  $\mathcal{H}'(\mathbf{k}')$ , can accurately predict the MZMs as obtained from the real space Hamiltonian under OBC (see Fig. 1 (c)). This correspondence for very higher values of  $\gamma$  no longer remains appropriate due to the possible break down of Eq. (2). Even though  $M_{x,y}$  are broken,  $\langle \nu_{y,\mu'}^{\pm\nu_x} \rangle$  ( $\langle \nu_{x,\mu'}^{\pm\nu_y} \rangle$ ) yields half-integer quantization provided  $\mathcal{M}_{xy}$  ( $\mathcal{M}_{\bar{x}\bar{y}}$ ) is preserved. Note that based on mirror rotation and sublattice symmetries, the NH SOTSC can be shown to exhibit integer quantization in winding number similar to NH SOTI [100] (see supplemental material [117]).

**Floquet generation of NH SOTSC.**— Having studied the static NH SOTSC, we seek the answer to engineer dynamic NH SOTSC out of trivial phase by periodically kicking the on-site mass term of the Hamiltonian  $\mathcal{H}(\mathbf{k})$  (Eq. (S1)) as [57, 64]

$$m(t) = m_1 \sum_{r=-\infty}^{\infty} \delta(t - rT). \quad (8)$$

Here,  $m_1$  and  $T$  represent the strength of the drive and the time-period, respectively. The Floquet operator is formulated to be

$$U(\mathbf{k}, T) = \text{TO} \exp \left[ -i \int_0^T dt \{ \mathcal{H}(\mathbf{k}) + m(t)\Gamma_3 \} \right] \\ = \exp[-i\mathcal{H}(\mathbf{k})T] \exp[-im_1\Gamma_3], \quad (9)$$

where TO denotes the time ordering. Notice that  $m_0 > |t_x + t_y + \sqrt{\gamma_x^2 + \gamma_y^2}|$  such that the underlying static NH Hamiltonian  $\mathcal{H}(\mathbf{k})$  remains in the trivially gapped phase. Having constructed the Floquet operator  $U(\mathbf{k}, T)$ , we resort to OBCs and diagonalize the Floquet operator to obtain the quasi-energy spectrum for the system. We depict the real part of the quasi-energy  $\mu_m$  as function of the state index  $m$  in Fig. 3 (a) where frequency of the drive is higher than the band-width of the system. The existence of eight MZMs is a signature of the NH Floquet SOTSC phase. The LDOS for the MZMs displays substantial localization only at one corner in Fig. 3(b).

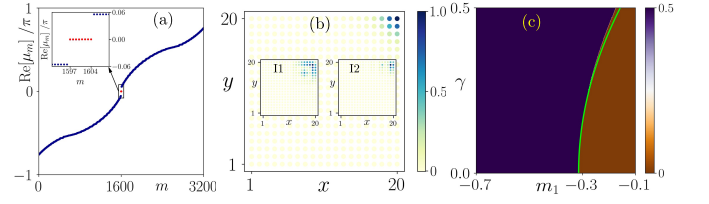


FIG. 3. (a) The real part of the quasi-energy spectrum  $E_m$ , obtained from Eq. (9) under OBC, are shown with eight Floquet Majorana 0-modes in the inset. (b) The LDOS, associated with eight MZMs in (a), exhibits substantial localization only at one corner similar to Fig. 2 (c). The LDOS for typical bulk modes with  $E_m = -0.697702\pi$  and  $-0.453177\pi$  are demonstrated in insets I1 and I2. (c) The topological phase diagram is depicted in the  $m_1$ - $\gamma$  plane where the Floquet SOTSC phase is characterized by the average Floquet nested Wannier sector polarization  $\langle \nu_{y,\mu'}^{\pm\nu_x} \rangle = 0.5$  (blue region). The phase boundary, marked by green line, is consistent with Eq. (11). We consider  $m_0 = 2.5$ ,  $m_1 = -0.4$ ,  $\Omega = 10.0$  such that we start from the trivial phase deep inside the brown region in Fig. 1 (c).

Insets show the NH skin effect where the bulk modes at finite energy also have a fair amount of corner localization.

In order to topologically characterize the above MZMs, we again make use of the non-Bloch form. Instead of the static Hamiltonian, we derive the high-frequency effective Floquet Hamiltonian, in the limit  $T \rightarrow 0$  and  $m_1 \rightarrow 0$  to analyze the situation

$$H_{\text{Flq}}(\mathbf{k}) \approx \mathcal{H}(\mathbf{k}) + \frac{m_1}{T} \Gamma_1 + m_1 \sum_{j=2}^4 N_j \Gamma_{j1}, \quad (10)$$

with  $\Gamma_{21} = -\sigma_y s_z$ ,  $\Gamma_{31} = \sigma_x$ ,  $\Gamma_{41} = -\tau_y \sigma_z$ . Upon substitution of  $\mathbf{k} \rightarrow \mathbf{k}' + i\beta$ , the modified mass term in  $H'_{\text{Flq}}(\mathbf{k}')$  reads as

$$m'_0 = m_0 - t_x - t_y - \frac{\gamma_x^2}{2\lambda_x^2} - \frac{\gamma_y^2}{2\lambda_y^2} + \frac{m_1}{T}. \quad (11)$$

Evaluating the effective Floquet nested Wannier sector polarization  $\langle \nu_{y,\mu'}^{\pm\nu_x} \rangle$  numerically from non-Bloch Floquet operator  $U'(\mathbf{k}', T)$  [48, 66], we obtain the Floquet phase diagram in  $m_1$ - $\gamma$  plane as shown in Fig. 3 (c). The non-Bloch Floquet operator can be considered as the dynamic analog of the non-Bloch NH Hamiltonian  $H'(\mathbf{k}')$ . In particular, we use bi-orthogonalized  $|\Psi_F^R(\mathbf{k}')\rangle$  ( $\langle \Psi_F^L(\mathbf{k}')|$ ), representing the occupied right (left) quasi-states of  $U'(\mathbf{k}', T)$  with quasi-energy  $-\pi/T < \text{Re}[\mu] < 0$ , to construct the Wilson loops  $W_{x,\mathbf{k}'}$  for the driven case. Following identical line of arguments, presented for the static case,  $W_{y,\mathbf{k}'}^{\pm\nu_x}$  is obtained from  $\left[ F_{y,\mathbf{k}'}^{\pm\nu_x} \right]_{\mu_1\mu_2} = \sum_{mn} \left[ \nu_{x,\mu_1}^{F,L}(\mathbf{k}' + \Delta_y \mathbf{e}_y) \right]_m^* \left[ F_{y,\mathbf{k}'}^F \right]_{mn} \left[ \nu_{x,\mu_2}^{F,R}(\mathbf{k}') \right]_n$  with  $\left[ F_{y,\mathbf{k}'}^F \right]_{mn} = \langle \Psi_{Fm}^L(\mathbf{k}' + \Delta_y \mathbf{e}_y) | \Psi_{Fn}^R(\mathbf{k}') \rangle$  and  $|\nu_{x,\mu}^{F,R}(\mathbf{k}')\rangle$  ( $\langle \nu_{x,\mu}^{F,L}(\mathbf{k}')|$ ) designates bi-orthogonalized right (left)



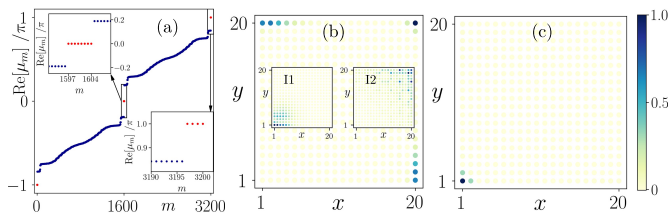


FIG. 4. (a) We repeat Fig. 3 (a) considering the low frequency mass-kick with  $\Omega = 5.0$  where we find eight regular 0- and anomalous  $\pi$ -modes simultaneously. We show the LDOS associated with  $\text{Re}[E_m] = 0-$  and  $\text{Re}[E_m] = +\pi$  in (b) and (c), respectively. The LDOS for Floquet bulk modes with  $E_m = -0.838779\pi - 0.085397\pi i$  and  $-0.471932\pi$  are respectively depicted in the insets I1 and I2 of (b). We consider  $m_0 = 0, m_1 = 1.5, \Omega = 5.0$ .

eigenvector of  $W_{x,\mathbf{k}}^F$ . Interestingly, this is similar to the static phase diagram where the phase boundary is accurately explained by Eq. (11).

We further analyze the problem for lower frequency regime to look for anomalous Floquet modes at quasienergy  $\text{Re}[\mu] = \pm\pi$  [57, 66]. We depict one such scenario for  $\Omega = 2\pi/T = 5.0$  in Fig. 4 (a) where eight anomalous  $\pi$ -modes appear simultaneously with regular eight 0-modes. The corresponding LDOS for 0-mode and  $\pi$ -mode are shown in Fig. 4(b) and (c), respectively. Interestingly, the 0-mode and the  $\pi$ -mode populate different corners of the system. As a signature of NH skin effect, we show the LDOS for two bulk states in the inset I1 and I2 of Fig. 4(b). The localization profile of the zero-energy states and bulk states are unique to the NH system that can not be explored in its Hermitian counterpart.

**Discussions.**— The number of MZMs can be tuned in our case by the application of magnetic field similar to the Hermitian SOTSC phase [64]. The long-range hopping provides another route to enhance the number of MZMs that can in principle be applicable for the non-Hermitian case as well [121, 122]. Interestingly, Floquet driving delivers an alternative handle to generate long-range hopping effectively out of the short-range NH model such that the number of MZMs are varied (see supplemental material [117]). Interestingly, Hermitian and non-Hermitian phases belong to the Dirac and non-Hermitian Dirac universality classes [123, 124]. In the case of HOT phases, one expects different critical exponents with re-

spect to the usual Dirac model. The breakdown of BBC and skin effect are intimately related to such non-Hermitian Dirac universality class. The edge theory, computed from Hermitian HOT model, is modified due to the non-Hermiticity with the possible non-Bloch form. Given the experimental realization of spin-orbit coupling [125, 126], non-Hermiticity [127, 128] and theoretical proposals on topological superfluidity [129, 130] in optical lattice, we believe that the cold atom systems might be a suitable platform for the potential experimental realization of our findings [74, 131, 132]. However, we note that the superconductivity might be hard to achieve in the NH setting.

**Summary and conclusions.**— In this article, we consider 2D NH TI, proximized with  $d$ -wave superconductivity, to investigate the emergence of NH SOTSC phase. From the analysis of EPs on the bulk NH Hamiltonian under PBC, one can estimate the gapped and gapless phase in terms of the real energies (see Fig. 1). By contrast, the MZMs, obtained from the real space NH Hamiltonian under OBC, do not immediately vanish inside the bulk gapless region (see Fig. 2). This apparent breakdown of the BBC can be explained by the non-Bloch nature of the NH Hamiltonian that further results in the MZMs residing at only one corner while the bulk modes populate the boundaries. While the later is dubbed as NH skin effect. We propose the nested polarization for topologically characterize the MZMs upon exploiting the non-Bloch form of the complex wave vectors. This resolves the anomaly between the phase boundaries, obtained from OBC and PBC, in the topological phase diagram. Finally, we adopt a mass-kick drive to illustrate the Floquet generation of NH SOTSC out of the trivial phase and characterize it using non-Bloch Floquet nested Wannier sector polarization (see Fig. 3). In addition, we demonstrate the emergence of anomalous  $\pi$ -mode following such drive when the frequency is lowered (see Fig. 4). The mirror symmetries  $M_{x,y}$  play crucial role in characterizing the anomalous  $\pi$ -modes [48, 66]. Therefore, such characterization in the absence of mirror symmetries is a future problem.

**Acknowledgments.**— A.K.G. acknowledges SAMKHYA: High-Performance Computing Facility provided by Institute of Physics, Bhubaneswar, for numerical computations. We thank Arijit Saha for useful discussions.

- 
- [1] M. Z. Hasan and C. L. Kane, “Colloquium: topological insulators,” *Rev. Mod. Phys.* **82**, 3045 (2010).
  - [2] F. D. M. Haldane, “Model for a quantum hall effect without landau levels: Condensed-matter realization of the “parity anomaly,”” *Phys. Rev. Lett.* **61**, 2015–2018 (1988).
  - [3] C. L. Kane and E. J. Mele, “ $Z_2$  topological order and the

- quantum spin hall effect,” *Phys. Rev. Lett.* **95**, 146802 (2005).
- [4] B. A. Bernevig, T. L. Hughes, and S.-C. Zhang, “Quantum spin hall effect and topological phase transition in hgte quantum wells,” *Science* **314**, 1757–1761 (2006).
- [5] J. Alicea, “New directions in the pursuit of majorana fermions in solid state systems,” *Rep. Prog. Phys.* **75**,

- 076501 (2012).
- [6] C. Beenakker, “Search for majorana fermions in superconductors,” *Annu. Rev. Condens. Matter Phys.* **4**, 113–136 (2013).
  - [7] G. Jotzu, M. Messer, R. Desbuquois, M. Lebrat, T. Uehlinger, D. Greif, and T. Esslinger, “Experimental realization of the topological haldane model with ultracold fermions,” *Nature* **515**, 237–240 (2014).
  - [8] A. Das, Y. Ronen, Y. Most, Y. Oreg, M. Heiblum, and H. Shtrikman, “Zero-bias peaks and splitting in an al<sub>in</sub>as nanowire topological superconductor as a signature of majorana fermions,” *Nat. Phys.* **8**, 887–895 (2012).
  - [9] W. A. Benalcazar, B. A. Bernevig, and T. L. Hughes, “Quantized electric multipole insulators,” *Science* **357**, 61–66 (2017).
  - [10] W. A. Benalcazar, B. A. Bernevig, and T. L. Hughes, “Electric multipole moments, topological multipole moment pumping, and chiral hinge states in crystalline insulators,” *Phys. Rev. B* **96**, 245115 (2017).
  - [11] Z. Song, Z. Fang, and C. Fang, “ $(d - 2)$ -dimensional edge states of rotation symmetry protected topological states,” *Phys. Rev. Lett.* **119**, 246402 (2017).
  - [12] J. Langbehn, Y. Peng, L. Trifunovic, F. von Oppen, and P. W. Brouwer, “Reflection-symmetric second-order topological insulators and superconductors,” *Phys. Rev. Lett.* **119**, 246401 (2017).
  - [13] F. Schindler, A. M. Cook, M. G. Vergniory, Z. Wang, S. S. Parkin, B. A. Bernevig, and T. Neupert, “Higher-order topological insulators,” *Science adv.* **4**, eaat0346 (2018).
  - [14] S. Franca, J. van den Brink, and I. C. Fulga, “An anomalous higher-order topological insulator,” *Phys. Rev. B* **98**, 201114 (2018).
  - [15] Z. Wang, B. J. Wieder, J. Li, B. Yan, and B. A. Bernevig, “Higher-order topology, monopole nodal lines, and the origin of large fermi arcs in transition metal dichalcogenides  $xte_2$  ( $x = \text{Mo}, \text{W}$ ),” *Phys. Rev. Lett.* **123**, 186401 (2019).
  - [16] D. Călugăru, V. Juričić, and B. Roy, “Higher-order topological phases: A general principle of construction,” *Phys. Rev. B* **99**, 041301 (2019).
  - [17] P. Szumniak, D. Loss, and J. Klinovaja, “Hinge modes and surface states in second-order topological three-dimensional quantum hall systems induced by charge density modulation,” *Phys. Rev. B* **102**, 125126 (2020).
  - [18] X. Ni, M. Li, M. Weiner, A. Alù, and A. B. Khanikaev, “Demonstration of a quantized acoustic octupole topological insulator,” *Nature Communications* **11**, 2108 (2020).
  - [19] B. Xie, H. Wang, X. Zhang, P. Zhan, J. Jiang, M. Lu, and Y. Chen, “Higher-order band topology,” *Nat. Rev. Phys.* **3**, 520–532 (2021).
  - [20] S. Saha, T. Nag, and S. Mandal, “Dipolar quantum spin hall insulator phase in extended haldane model,” (2022), [arXiv:2204.06641](https://arxiv.org/abs/2204.06641).
  - [21] X. Zhu, “Tunable majorana corner states in a two-dimensional second-order topological superconductor induced by magnetic fields,” *Phys. Rev. B* **97**, 205134 (2018).
  - [22] T. Liu, J. J. He, and F. Nori, “Majorana corner states in a two-dimensional magnetic topological insulator on a high-temperature superconductor,” *Phys. Rev. B* **98**, 245413 (2018).
  - [23] Z. Yan, F. Song, and Z. Wang, “Majorana corner modes in a high-temperature platform,” *Phys. Rev. Lett.* **121**, 096803 (2018).
  - [24] Y. Wang, M. Lin, and T. L. Hughes, “Weak-pairing higher order topological superconductors,” *Phys. Rev. B* **98**, 165144 (2018).
  - [25] R.-X. Zhang, W. S. Cole, and S. Das Sarma, “Helical hinge majorana modes in iron-based superconductors,” *Phys. Rev. Lett.* **122**, 187001 (2019).
  - [26] R.-X. Zhang, W. S. Cole, X. Wu, and S. Das Sarma, “Higher-order topology and nodal topological superconductivity in fe(se,te) heterostructures,” *Phys. Rev. Lett.* **123**, 167001 (2019).
  - [27] Y. Volpez, D. Loss, and J. Klinovaja, “Second-order topological superconductivity in  $\pi$ -junction rashba layers,” *Phys. Rev. Lett.* **122**, 126402 (2019).
  - [28] Z. Yan, “Majorana corner and hinge modes in second-order topological insulator/superconductor heterostructures,” *Phys. Rev. B* **100**, 205406 (2019).
  - [29] S. A. A. Ghorashi, X. Hu, T. L. Hughes, and E. Rossi, “Second-order dirac superconductors and magnetic field induced majorana hinge modes,” *Phys. Rev. B* **100**, 020509 (2019).
  - [30] Y.-J. Wu, J. Hou, Y.-M. Li, X.-W. Luo, X. Shi, and C. Zhang, “In-plane zeeman-field-induced majorana corner and hinge modes in an  $s$ -wave superconductor heterostructure,” *Phys. Rev. Lett.* **124**, 227001 (2020).
  - [31] K. Laubscher, D. Chughtai, D. Loss, and J. Klinovaja, “Kramers pairs of majorana corner states in a topological insulator bilayer,” *Phys. Rev. B* **102**, 195401 (2020).
  - [32] B. Roy, “Higher-order topological superconductors in  $\mathcal{P}$ -,  $\mathcal{T}$ -odd quadrupolar dirac materials,” *Phys. Rev. B* **101**, 220506 (2020).
  - [33] S.-B. Zhang, W. B. Rui, A. Calzona, S.-J. Choi, A. P. Schnyder, and B. Trauzettel, “Topological and holo-nomic quantum computation based on second-order topological superconductors,” *Phys. Rev. Research* **2**, 043025 (2020).
  - [34] M. Kheirkhah, Z. Yan, and F. Marsiglio, “Vortex-line topology in iron-based superconductors with and without second-order topology,” *Phys. Rev. B* **103**, L140502 (2021).
  - [35] Z. Yan, “Higher-order topological odd-parity superconductors,” *Phys. Rev. Lett.* **123**, 177001 (2019).
  - [36] J. Ahn and B.-J. Yang, “Higher-order topological superconductivity of spin-polarized fermions,” *Phys. Rev. Research* **2**, 012060 (2020).
  - [37] X.-J. Luo, X.-H. Pan, and X. Liu, “Higher-order topological superconductors based on weak topological insulators,” *Phys. Rev. B* **104**, 104510 (2021).
  - [38] Q. Wang, C.-C. Liu, Y.-M. Lu, and F. Zhang, “High-temperature majorana corner states,” *Phys. Rev. Lett.* **121**, 186801 (2018).
  - [39] A. K. Ghosh, T. Nag, and A. Saha, “Hierarchy of higher-order topological superconductors in three dimensions,” *Phys. Rev. B* **104**, 134508 (2021).
  - [40] B. Roy and V. Juričić, “Mixed-parity octupolar pairing and corner majorana modes in three dimensions,” *Phys. Rev. B* **104**, L180503 (2021).
  - [41] T. Li, M. Geier, J. Ingham, and H. D. Scammell, “Higher-order topological superconductivity from repulsive interactions in kagome and honeycomb systems,” *2D Materials* **9**, 015031 (2021).
  - [42] R. W. Bomantara, L. Zhou, J. Pan, and J. Gong, “Coupled-wire construction of static and floquet second-


- order topological insulators,” *Phys. Rev. B* **99**, 045441 (2019).
- [43] T. Nag, V. Juričić, and B. Roy, “Out of equilibrium higher-order topological insulator: Floquet engineering and quench dynamics,” *Phys. Rev. Research* **1**, 032045 (2019).
- [44] Y. Peng and G. Refael, “Floquet second-order topological insulators from nonsymmorphic space-time symmetries,” *Phys. Rev. Lett.* **123**, 016806 (2019).
- [45] R. Seshadri, A. Dutta, and D. Sen, “Generating a second-order topological insulator with multiple corner states by periodic driving,” *Phys. Rev. B* **100**, 115403 (2019).
- [46] M. Rodriguez-Vega, A. Kumar, and B. Seradjeh, “Higher-order floquet topological phases with corner and bulk bound states,” *Phys. Rev. B* **100**, 085138 (2019).
- [47] A. K. Ghosh, G. C. Paul, and A. Saha, “Higher order topological insulator via periodic driving,” *Phys. Rev. B* **101**, 235403 (2020).
- [48] B. Huang and W. V. Liu, “Floquet higher-order topological insulators with anomalous dynamical polarization,” *Phys. Rev. Lett.* **124**, 216601 (2020).
- [49] H. Hu, B. Huang, E. Zhao, and W. V. Liu, “Dynamical singularities of floquet higher-order topological insulators,” *Phys. Rev. Lett.* **124**, 057001 (2020).
- [50] Y. Peng, “Floquet higher-order topological insulators and superconductors with space-time symmetries,” *Phys. Rev. Research* **2**, 013124 (2020).
- [51] T. Nag, V. Juričić, and B. Roy, “Hierarchy of higher-order floquet topological phases in three dimensions,” *Phys. Rev. B* **103**, 115308 (2021).
- [52] R.-X. Zhang and Z.-C. Yang, “Tunable fragile topology in floquet systems,” *Phys. Rev. B* **103**, L121115 (2021).
- [53] R. V. Bhat and S. Bera, “Out of equilibrium chiral higher order topological insulator on a  $\pi$ -flux square lattice,” *J. Phys. Condens. Matter* **33**, 164005 (2021).
- [54] W. Zhu, Y. D. Chong, and J. Gong, “Floquet higher-order topological insulator in a periodically driven bipartite lattice,” *Phys. Rev. B* **103**, L041402 (2021).
- [55] J. Yu, R.-X. Zhang, and Z.-D. Song, “Dynamical symmetry indicators for floquet crystals,” *Nature Communications* **12**, 5985 (2021).
- [56] D. Vu, “Dynamic bulk-boundary correspondence for anomalous floquet topology,” *Phys. Rev. B* **105**, 064304 (2022).
- [57] A. K. Ghosh, T. Nag, and A. Saha, “Systematic generation of the cascade of anomalous dynamical first- and higher-order modes in floquet topological insulators,” *Phys. Rev. B* **105**, 115418 (2022).
- [58] X.-L. Du, R. Chen, R. Wang, and D.-H. Xu, “Weyl nodes with higher-order topology in an optically driven nodal-line semimetal,” *Phys. Rev. B* **105**, L081102 (2022).
- [59] Z. Ning, B. Fu, D.-H. Xu, and R. Wang, “Tailoring quadrupole topological insulators with periodic driving and disorder,” (2022), [arXiv:2201.02414](https://arxiv.org/abs/2201.02414).
- [60] K. Plekhanov, M. Thakurathi, D. Loss, and J. Klinovaja, “Floquet second-order topological superconductor driven via ferromagnetic resonance,” *Phys. Rev. Research* **1**, 032013 (2019).
- [61] R. W. Bomantara and J. Gong, “Measurement-only quantum computation with floquet majorana corner modes,” *Phys. Rev. B* **101**, 085401 (2020).
- [62] R. W. Bomantara, “Time-induced second-order topological superconductors,” *Phys. Rev. Research* **2**, 033495 (2020).
- [63] A. K. Ghosh, T. Nag, and A. Saha, “Floquet generation of a second-order topological superconductor,” *Phys. Rev. B* **103**, 045424 (2021).
- [64] A. K. Ghosh, T. Nag, and A. Saha, “Floquet second order topological superconductor based on unconventional pairing,” *Phys. Rev. B* **103**, 085413 (2021).
- [65] D. Vu, R.-X. Zhang, Z.-C. Yang, and S. Das Sarma, “Superconductors with anomalous floquet higher-order topology,” *Phys. Rev. B* **104**, L140502 (2021).
- [66] A. K. Ghosh, T. Nag, and A. Saha, “Dynamical construction of quadrupolar and octupolar topological superconductors,” *Phys. Rev. B* **105**, 155406 (2022).
- [67] N. Parappurath, F. Alpegiani, L. Kuipers, and E. Verhagen, “Direct observation of topological edge states in silicon photonic crystals: Spin, dispersion, and chiral routing,” *Science Advances* **6**, eaaw4137 (2020).
- [68] Y. Yang, Z. Gao, H. Xue, L. Zhang, M. He, Z. Yang, R. Singh, Y. Chong, B. Zhang, and H. Chen, “Realization of a three-dimensional photonic topological insulator,” *Nature* **565**, 622–626 (2019).
- [69] S. Malzard, C. Poli, and H. Schomerus, “Topologically protected defect states in open photonic systems with non-hermitian charge-conjugation and parity-time symmetry,” *Phys. Rev. Lett.* **115**, 200402 (2015).
- [70] A. Regensburger, C. Bersch, M.-A. Miri, G. Onishchukov, D. N. Christodoulides, and U. Peschel, “Parity-time synthetic photonic lattices,” *Nature* **488**, 167–171 (2012).
- [71] R. El-Ganainy, K. G. Makris, M. Khajavikhan, Z. H. Musslimani, S. Rotter, and D. N. Christodoulides, “Non-hermitian physics and pt symmetry,” *Nature Physics* **14**, 11–19 (2018).
- [72] M. M. Denner, A. Skurativska, F. Schindler, M. H. Fischer, R. Thomale, T. Bzdušek, and T. Neupert, “Exceptional topological insulators,” *Nature Communications* **12**, 5681 (2021).
- [73] Z. H. Musslimani, K. G. Makris, R. El-Ganainy, and D. N. Christodoulides, “Optical solitons in  $\mathcal{PT}$  periodic potentials,” *Phys. Rev. Lett.* **100**, 030402 (2008).
- [74] K. G. Makris, R. El-Ganainy, D. N. Christodoulides, and Z. H. Musslimani, “Beam dynamics in  $\mathcal{PT}$  symmetric optical lattices,” *Phys. Rev. Lett.* **100**, 103904 (2008).
- [75] E. J. Bergholtz and J. C. Budich, “Non-hermitian weyl physics in topological insulator ferromagnet junctions,” *Phys. Rev. Research* **1**, 012003 (2019).
- [76] K. Yang, S. C. Morampudi, and E. J. Bergholtz, “Exceptional spin liquids from couplings to the environment,” *Phys. Rev. Lett.* **126**, 077201 (2021).
- [77] P. San-Jose, J. Cayao, E. Prada, and R. Aguado, “Majorana bound states from exceptional points in non-topological superconductors,” *Scientific Reports* **6**, 21427 (2016).
- [78] V. Kozi and L. Fu, “Non-hermitian topological theory of finite-lifetime quasiparticles: prediction of bulk fermi arc due to exceptional point,” [arXiv:1708.05841](https://arxiv.org/abs/1708.05841).
- [79] T. Yoshida, R. Peters, and N. Kawakami, “Non-hermitian perspective of the band structure in heavy-fermion systems,” *Phys. Rev. B* **98**, 035141 (2018).
- [80] H. Shen and L. Fu, “Quantum oscillation from in-gap states and a non-hermitian landau level problem,” *Phys.*

- Rev. Lett.* **121**, 026403 (2018).
- [81] S. Yao, F. Song, and Z. Wang, “Non-hermitian chern bands,” *Phys. Rev. Lett.* **121**, 136802 (2018).
  - [82] K. Kawabata, K. Shiozaki, M. Ueda, and M. Sato, “Symmetry and topology in non-hermitian physics,” *Phys. Rev. X* **9**, 041015 (2019).
  - [83] E. J. Bergholtz, J. C. Budich, and F. K. Kunst, “Exceptional topology of non-hermitian systems,” *Rev. Mod. Phys.* **93**, 015005 (2021).
  - [84] K. Sone, Y. Ashida, and T. Sagawa, “Exceptional non-hermitian topological edge mode and its application to active matter,” *Nature Communications* **11**, 5745 (2020).
  - [85] C. M. Bender, “Making sense of non-hermitian hamiltonians,” *Rep. Prog. Phys.* **70**, 947–1018 (2007).
  - [86] W. D. Heiss, “The physics of exceptional points,” *J. Phys. A: Math. Theor.* **45**, 444016 (2012).
  - [87] S. Yao and Z. Wang, “Edge states and topological invariants of non-hermitian systems,” *Phys. Rev. Lett.* **121**, 086803 (2018).
  - [88] F. K. Kunst, E. Edvardsson, J. C. Budich, and E. J. Bergholtz, “Biorthogonal bulk-boundary correspondence in non-hermitian systems,” *Phys. Rev. Lett.* **121**, 026808 (2018).
  - [89] T. Helbig, T. Hofmann, S. Imhof, M. Abdelghany, T. Kiessling, L. W. Molenkamp, C. H. Lee, A. Szameit, M. Greiter, and R. Thomale, “Generalized bulk-boundary correspondence in non-hermitian topoelectrical circuits,” *Nature Physics* **16**, 747–750 (2020).
  - [90] D. S. Borgnia, A. J. Kruchkov, and R.-J. Slager, “Non-hermitian boundary modes and topology,” *Phys. Rev. Lett.* **124**, 056802 (2020).
  - [91] R. Koch and J. C. Budich, “Bulk-boundary correspondence in non-hermitian systems: stability analysis for generalized boundary conditions,” *The European Physical Journal D* **74**, 70 (2020).
  - [92] H.-G. Zirnstein, G. Refael, and B. Rosenow, “Bulk-boundary correspondence for non-hermitian hamiltonians via green functions,” *Phys. Rev. Lett.* **126**, 216407 (2021).
  - [93] Y. Takane, “Bulk-boundary correspondence in a non-hermitian chern insulator,” *Journal of the Physical Society of Japan* **90**, 033704 (2021).
  - [94] K. Kawabata, M. Sato, and K. Shiozaki, “Higher-order non-hermitian skin effect,” *Phys. Rev. B* **102**, 205118 (2020).
  - [95] K. Zhang, Z. Yang, and C. Fang, “Correspondence between winding numbers and skin modes in non-hermitian systems,” *Phys. Rev. Lett.* **125**, 126402 (2020).
  - [96] Z. Gong, Y. Ashida, K. Kawabata, K. Takasan, S. Higashikawa, and M. Ueda, “Topological phases of non-hermitian systems,” *Phys. Rev. X* **8**, 031079 (2018).
  - [97] C. Yin, H. Jiang, L. Li, R. Lü, and S. Chen, “Geometrical meaning of winding number and its characterization of topological phases in one-dimensional chiral non-hermitian systems,” *Phys. Rev. A* **97**, 052115 (2018).
  - [98] A. Banerjee and A. Narayan, “Controlling exceptional points with light,” *Phys. Rev. B* **102**, 205423 (2020).
  - [99] D. Chowdhury, A. Banerjee, and A. Narayan, “Light-driven lifshitz transitions in non-hermitian multi-weyl semimetals,” *Phys. Rev. A* **103**, L051101 (2021).
  - [100] T. Liu, Y.-R. Zhang, Q. Ai, Z. Gong, K. Kawabata, M. Ueda, and F. Nori, “Second-order topological phases in non-hermitian systems,” *Phys. Rev. Lett.* **122**, 076801 (2019).
  - [101] X.-W. Luo and C. Zhang, “Higher-order topological corner states induced by gain and loss,” *Phys. Rev. Lett.* **123**, 073601 (2019).
  - [102] E. Edvardsson, F. K. Kunst, and E. J. Bergholtz, “Non-hermitian extensions of higher-order topological phases and their biorthogonal bulk-boundary correspondence,” *Phys. Rev. B* **99**, 081302 (2019).
  - [103] Z. Zhang, M. Rosendo López, Y. Cheng, X. Liu, and J. Christensen, “Non-hermitian sonic second-order topological insulator,” *Phys. Rev. Lett.* **122**, 195501 (2019).
  - [104] C. H. Lee, L. Li, and J. Gong, “Hybrid higher-order skin-topological modes in nonreciprocal systems,” *Phys. Rev. Lett.* **123**, 016805 (2019).
  - [105] Y.-J. Wu, C.-C. Liu, and J. Hou, “Wannier-type photonic higher-order topological corner states induced solely by gain and loss,” *Phys. Rev. A* **101**, 043833 (2020).
  - [106] R. Okugawa, R. Takahashi, and K. Yokomizo, “Second-order topological non-hermitian skin effects,” *Phys. Rev. B* **102**, 241202 (2020).
  - [107] R. Okugawa, R. Takahashi, and K. Yokomizo, “Non-hermitian band topology with generalized inversion symmetry,” *Phys. Rev. B* **103**, 205205 (2021).
  - [108] K. Shiozaki and S. Ono, “Symmetry indicator in non-hermitian systems,” *Phys. Rev. B* **104**, 035424 (2021).
  - [109] Y. Yu, M. Jung, and G. Shvets, “Zero-energy corner states in a non-hermitian quadrupole insulator,” *Phys. Rev. B* **103**, L041102 (2021).
  - [110] N. Okuma and M. Sato, “Topological phase transition driven by infinitesimal instability: Majorana fermions in non-hermitian spintronics,” *Phys. Rev. Lett.* **123**, 097701 (2019).
  - [111] S. Lieu, “Non-hermitian majorana modes protect degenerate steady states,” *Phys. Rev. B* **100**, 085110 (2019).
  - [112] J. Avila, F. Peñaranda, E. Prada, P. San-Jose, and R. Aguado, “Non-hermitian topology as a unifying framework for the andreev versus majorana states controversy,” *Communications Physics* **2**, 133 (2019).
  - [113] X.-M. Zhao, C.-X. Guo, M.-L. Yang, H. Wang, W.-M. Liu, and S.-P. Kou, “Anomalous non-abelian statistics for non-hermitian generalization of majorana zero modes,” *Phys. Rev. B* **104**, 214502 (2021).
  - [114] Z.-H. Wang, F. Xu, L. Li, D.-H. Xu, W.-Q. Chen, and B. Wang, “Majorana polarization in non-hermitian topological superconductors,” *Phys. Rev. B* **103**, 134507 (2021).
  - [115] H. Liu, M. Lu, Y. Wu, J. Liu, and X. C. Xie, “Non-hermiticity stabilized majorana zero modes in semiconductor-superconductor nanowires,” (2021), [arXiv:2111.11731](https://arxiv.org/abs/2111.11731).
  - [116] L. Zhou, “Non-hermitian floquet topological superconductors with multiple majorana edge modes,” *Phys. Rev. B* **101**, 014306 (2020).
  - [117] See Supplemental Material at XXXX-XXXX for discussions on underlying symmetry of the model, localization of MZMs for the asymmetry in the non-hermiticity, symmetry constraint of Wannier band, effect of disorder, and tuning the number of MCMs dynamically.
  - [118] O. Viyuela, D. Vodola, G. Pupillo, and M. A. Martin-Delgado, “Topological massive dirac edge modes and long-range superconducting hamiltonians,” *Phys. Rev.*



- B **94**, 125121 (2016).
- [119] H. Shen, B. Zhen, and L. Fu, “Topological band theory for non-hermitian hamiltonians,” *Phys. Rev. Lett.* **120**, 146402 (2018).
  - [120] K. Esaki, M. Sato, K. Hasebe, and M. Kohmoto, “Edge states and topological phases in non-hermitian systems,” *Phys. Rev. B* **84**, 205128 (2011).
  - [121] W. DeGottardi, M. Thakurathi, S. Vishveshwara, and D. Sen, “Majorana fermions in superconducting wires: Effects of long-range hopping, broken time-reversal symmetry, and potential landscapes,” *Phys. Rev. B* **88**, 165111 (2013).
  - [122] W. A. Benalcazar and A. Cerjan, “Chiral-symmetric higher-order topological phases of matter,” *Phys. Rev. Lett.* **128**, 127601 (2022).
  - [123] W. Chen, M. Legner, A. Rüegg, and M. Sigrist, “Correlation length, universality classes, and scaling laws associated with topological phase transitions,” *Phys. Rev. B* **95**, 075116 (2017).
  - [124] R. Arouca, C. H. Lee, and C. Morais Smith, “Unconventional scaling at non-hermitian critical points,” *Phys. Rev. B* **102**, 245145 (2020).
  - [125] L. Huang, Z. Meng, P. Wang, P. Peng, S.-L. Zhang, L. Chen, D. Li, Q. Zhou, and J. Zhang, “Experimental realization of two-dimensional synthetic spin-orbit coupling in ultracold fermi gases,” *Nature Physics* **12**, 540–544 (2016).
  - [126] Z. Wu, L. Zhang, W. Sun, X.-T. Xu, B.-Z. Wang, S.-C. Ji, Y. Deng, S. Chen, X.-J. Liu, and J.-W. Pan, “Realization of two-dimensional spin-orbit coupling for bose-einstein condensates,” *Science* **354**, 83–88 (2016).
  - [127] J. Li, A. K. Harter, J. Liu, L. de Melo, Y. N. Joglekar, and L. Luo, “Observation of parity-time symmetry breaking transitions in a dissipative floquet system of ultracold atoms,” *Nature communications* **10**, 855 (2019).
  - [128] W. Song, W. Sun, C. Chen, Q. Song, S. Xiao, S. Zhu, and T. Li, “Breakup and recovery of topological zero modes in finite non-hermitian optical lattices,” *Phys. Rev. Lett.* **123**, 165701 (2019).
  - [129] W. Jia, Z.-H. Huang, X. Wei, Q. Zhao, and X.-J. Liu, “Topological superfluids for spin-orbit coupled ultracold fermi gases,” *Phys. Rev. B* **99**, 094520 (2019).
  - [130] A. Bühler, N. Lang, C. V. Kraus, G. Möller, S. D. Huber, and H.-P. Büchler, “Majorana modes and p-wave superfluids for fermionic atoms in optical lattices,” *Nature communications* **5**, 4504 (2014).
  - [131] H. Miyake, G. A. Siviloglou, C. J. Kennedy, W. C. Burton, and W. Ketterle, “Realizing the harper hamiltonian with laser-assisted tunneling in optical lattices,” *Phys. Rev. Lett.* **111**, 185302 (2013).
  - [132] D. McKay and B. DeMarco, “Cooling in strongly correlated optical lattices: prospects and challenges,” *Reports on Progress in Physics* **74**, 054401 (2011).
  - [133] C.-K. Chiu, J. C. Y. Teo, A. P. Schnyder, and S. Ryu, “Classification of topological quantum matter with symmetries,” *Rev. Mod. Phys.* **88**, 035005 (2016).

# Supplemental Material for “Non-Hermitian higher-order topological superconductors in two-dimension: statics and dynamics”

Arnob Kumar Ghosh <sup>1,2</sup>, and Tanay Nag <sup>3</sup>

<sup>1</sup>*Institute of Physics, Sachivalaya Marg, Bhubaneswar-751005, India*

<sup>2</sup>*Homi Bhabha National Institute, Training School Complex, Anushakti Nagar, Mumbai 400094, India*

<sup>3</sup>*Department of Physics and Astronomy, Uppsala University, Box 516, 75120 Uppsala, Sweden*

## S1. UNDERLYING SPATIAL SYMMETRY

In this section, we analyze the crystalline symmetries associated with the non-Hermitian (NH) second-order topological superconductor (SOTSC) as presented in Eq. (1) of the main text. In order to understand the spatial symmetry of the model, we first analyze the underlying Hermitian version of our model  $\mathcal{H}^H(\mathbf{k}) = \lambda_x \sin k_x \tau_z \sigma_x s_z + \lambda_y \sin k_y \tau_z \sigma_y s_0 + (m_0 - t_x \cos k_x - t_y \cos k_y) \tau_z \sigma_z s_0 + \Delta(\cos k_x - \cos k_y) \tau_x \sigma_0 s_0$  as demonstrated in Eq. (1) of the main text. The Hermitian Hamiltonian obeys the following spatial symmetries-

- mirror symmetry along  $x$  with  $\mathcal{M}_x = \tau_x \sigma_x s_0$ :  $\mathcal{M}_x \mathcal{H}^H(k_x, k_y) \mathcal{M}_x^{-1} = \mathcal{H}^H(-k_x, k_y)$ ,
- mirror symmetry along  $y$  with  $\mathcal{M}_y = \tau_y \sigma_y s_0$ :  $\mathcal{M}_y \mathcal{H}^H(k_x, k_y) \mathcal{M}_y^{-1} = \mathcal{H}^H(k_x, -k_y)$ ,
- four-fold rotation with  $C_4 = \tau_z e^{-\frac{i\pi}{4} \sigma_z s_z}$ :  $C_4 \mathcal{H}^H(k_x, k_y) C_4^{-1} = \mathcal{H}^H(-k_y, k_x)$ , if  $t_x = t_y$  and  $\lambda_x = \lambda_y$ ,
- mirror rotation I with  $\mathcal{M}_{xy} = C_4 \mathcal{M}_y$ :  $\mathcal{M}_{xy} \mathcal{H}^H(k_x, k_y) \mathcal{M}_{xy}^{-1} = \mathcal{H}^H(k_y, k_x)$ , if  $t_x = t_y$  and  $\lambda_x = \lambda_y$ ,
- mirror rotation II with  $\mathcal{M}_{x\bar{y}} = C_4 \mathcal{M}_x$ :  $\mathcal{M}_{x\bar{y}} \mathcal{H}^H(k_x, k_y) \mathcal{M}_{x\bar{y}}^{-1} = \mathcal{H}^H(-k_y, -k_x)$ , if  $t_x = t_y$  and  $\lambda_x = \lambda_y$ ,
- sublattice/ chiral symmetry with  $\mathcal{S} = \tau_y \sigma_0 s_0$ :  $\mathcal{S} \mathcal{H}^H(\mathbf{k}) \mathcal{S}^{-1} = -\mathcal{H}^H(\mathbf{k})$ .

The extended Hermitian Hamiltonian  $\tilde{\mathcal{H}}(\mathbf{k})$  is found to be crucial for analyzing the crystalline symmetries of the NH Hamiltonian that can be written as follows [94]

$$\tilde{\mathcal{H}}(\mathbf{k}) = \begin{pmatrix} 0 & \mathcal{H}(\mathbf{k}) \\ \mathcal{H}(\mathbf{k})^\dagger & 0 \end{pmatrix}. \quad (\text{S1})$$

To be precise,  $\tilde{\mathcal{H}}(\mathbf{k}) = \lambda_x \sin k_x \mu_x \tau_z \sigma_x s_z + \gamma_x \mu_y \tau_z \sigma_x s_z + \lambda_y \sin k_y \mu_x \tau_z \sigma_y s_0 + \gamma_y \mu_y \tau_z \sigma_y s_0 + (m_0 - t_x \cos k_x - t_y \cos k_y) \mu_x \tau_z \sigma_z s_0 + \Delta(\cos k_x - \cos k_y) \mu_x \tau_x \sigma_0 s_0$ . For  $\gamma_x \neq 0, \gamma_y = 0$  ( $\gamma_x = 0, \gamma_y \neq 0$ ),  $\tilde{\mathcal{H}}(\mathbf{k})$  breaks  $\mathcal{M}_x = \mu_x \tau_x \sigma_x s_0$  ( $\mathcal{M}_y = \mu_x \tau_x \sigma_y s_0$ ). When  $\gamma_x \neq 0, \gamma_y \neq 0$ ,  $\tilde{\mathcal{H}}(\mathbf{k})$  breaks  $C_4 = \mu_x \tau_z e^{-\frac{i\pi}{4} \sigma_z s_z}$ . For  $\gamma_x = \gamma_y \neq 0$ ,  $\tilde{\mathcal{H}}(\mathbf{k})$  preserves  $\mathcal{M}_{xy} = C_4 \mathcal{M}_y$  and  $\mathcal{M}_{x\bar{y}} = C_4 \mathcal{M}_x$ . On the other hand,  $\tilde{\mathcal{H}}(\mathbf{k})$  preserves the chiral symmetry  $\mathcal{S} = \mu_0 \tau_y \sigma_0 s_0$ .

Therefore, the NH Hamiltonian (Eq. (1) of the main text) breaks and respects the following symmetries. When  $\gamma_x \neq 0$  ( $\gamma_y \neq 0$ )  $\mathcal{H}(\mathbf{k})$  breaks  $\mathcal{M}_x$  ( $\mathcal{M}_y$ ) and when both  $\gamma_{x,y} \neq 0$ ,  $\mathcal{H}(\mathbf{k})$  breaks  $C_4$  symmetry. The Hamiltonian  $\mathcal{H}(\mathbf{k})$  obeys both  $\mathcal{M}_{xy}$  and  $\mathcal{M}_{x\bar{y}}$  provided  $\gamma_x = \gamma_y$ .  $\mathcal{H}(\mathbf{k})$  also preserves the sublattice/ chiral symmetry  $\mathcal{S}$  like its Hermitian counterpart.

## S2. EFFECT OF ASYMMETRIC $\gamma$ AND THE LOCALIZATION OF THE MAJORANA ZERO-MODES

In this section, we study the localization of the Majorana zero-modes (MZMs) for different values of  $\gamma_x$  and  $\gamma_y$  [100]. In Fig. 2 (c) of the main text, we demonstrate that the MZMs are located only at the top-right corner of the system when  $\gamma_x = \gamma_y = \gamma$ . However, one can choose  $\gamma_x = -\gamma_y = \gamma$  ( $\gamma_y = -\gamma_x = \gamma$ ), and following the calculation of the local density of states (LDOS), it turns out that the MZMs are now localized at the bottom-right [Fig. S1 (a)] (top-left [Fig. S1 (b)]) corner of the system. When  $\gamma_x = \gamma_y = -\gamma$ , the MZMs are localized at the bottom-left corner of the system [see Fig. S1 (c)]. However, if we break the mirror rotation symmetry  $\mathcal{M}_{xy}$  by considering  $\gamma_x \neq \gamma_y$ , we depict that the MZMs are localized at more than one corner of the system in Fig. S1 (d) and (e). We obtain a non-quantized value for the topological invariant defined by employing the nested Wilson loop in the main text [Eq.(7)] when the mirror-rotation symmetry  $\mathcal{M}_{xy}$  is broken. We can find that either right(left)-bottom or left(right)-top corner is only occupied for mirror-rotation symmetry  $\mathcal{M}_{x\bar{y}}$  ( $\mathcal{M}_{xy}$ ). Therefore, the localization profile of MZMs over a given corner is caused by the interplay between the mirror-rotation symmetry and non-Hermiticity [100].

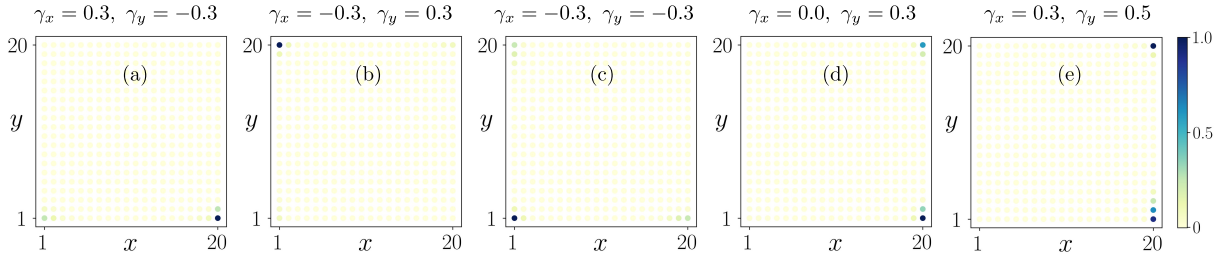


FIG. S1. We depict the local density of states for the Majorana zero-modes as a function of the system dimensions in (a) for  $\gamma_x = -\gamma_y = 0.3$ , (b) for  $\gamma_y = -\gamma_x = 0.3$ , (c) for  $\gamma_x = \gamma_y = -0.3$ , (d) for  $\gamma_x = 0.0, \gamma_y = 0.3$ , and (e) for  $\gamma_x = 0.3, \gamma_y = 0.5$ . The other parameters used here are  $t_x = t_y = \lambda_x = \lambda_y = \Delta = 1.0$ .

### S3. SYMMETRY CONSTRAINTS FOR WANNIER BANDS

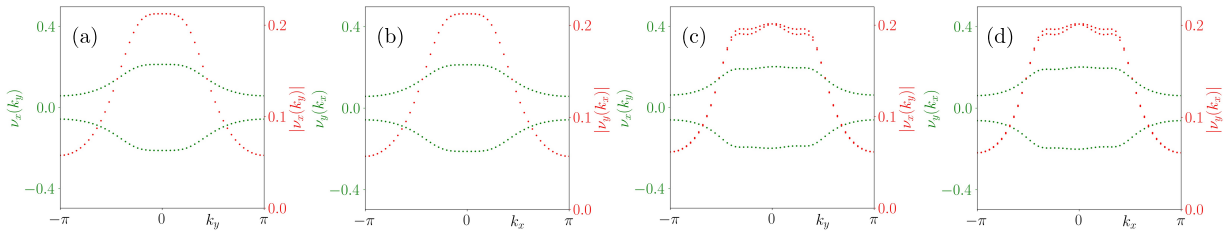


FIG. S2. We exhibit the first-order Wannier centres  $\nu_x(k_y)$  (left axis) and  $|\nu_x(k_y)|$  (right axis) as function of  $k_y$  in (a) for Hermitian case (c) for non-Hermitian case. In the non-Hermitian case the breaking of mirror symmetry  $M_x$  causes the irreversible nature of first-order branches *i.e.*,  $\nu_x(k_y) \not\rightarrow -\nu_x(k_y)$ , which is more evident from  $|\nu_x(k_y)|$ . (b), (d) We repeat (a) and (b) for  $\nu_y(k_x)$ . Note that for better visibility, we adopt the scale for  $\nu_x(k_y)$ ,  $\nu_y(k_x)$  to be between  $[-0.5, 0.5]$  while  $|\nu_x(k_y)|$ ,  $|\nu_y(k_x)|$  are bounded between  $[0.0, 0.22]$ .

In this section, we show that how the first- and second-order Wannier centres behave under the above spatial symmetries. The first-order Wannier centres  $\nu_x(k_y)$  and second-order Wannier centres  $\nu_y^{\nu_x}$  behave in the following way [10]– mirror-rotation along  $x$ -direction  $M_x$ :  $\nu_x(k_y) \rightarrow -\nu_x(k_y)$  [see Fig. S2], and  $\nu_y^{\nu_x}(k_x) \rightarrow \nu_y^{\nu_x}(-k_x)$ ;  $M_x$  causes the first-order branches to appear in pairs, mirror-rotation along  $y$ -direction.  $M_y$ :  $\nu_x(k_y) \rightarrow \nu_x(-k_y)$ , and  $\nu_y^{\nu_x}(k_x) \rightarrow -\nu_y^{\nu_x}(k_x)$ ;  $M_y$  defines the shape of the first-order branches. The four-fold rotation  $C_4$  and mirror rotations  $\mathcal{M}_{xy}$ ,  $\mathcal{M}_{x\bar{y}}$  interchange the branches,  $C_4$ :  $\nu_x(k_y) \rightarrow -\nu_y(k_x)$ , and  $\nu_y^{\nu_x}(k_x) \rightarrow \nu_x^{\nu_y}(-k_y)$ ,  $\mathcal{M}_{xy}$ :  $\nu_x(k_y) \rightarrow \nu_y(k_x)$ , and  $\nu_y^{\nu_x}(k_x) \rightarrow \nu_x^{\nu_y}(k_y)$   $\mathcal{M}_{x\bar{y}}$ :  $\nu_x(k_y) \rightarrow -\nu_y(-k_x)$ , and  $\nu_y^{\nu_x}(k_x) \rightarrow -\nu_x^{\nu_y}(-k_y)$ . In our case, the first-order branches do not follow the above relations as  $M_{x,y}$  symmetries are broken. However, the second-order polarization *i.e.*, nested polarization  $\text{mod}(\langle \nu_{y,\mu'}^{\pm \nu_x} \rangle, 1.0)$  and  $\text{mod}(\langle \nu_{x,\mu'}^{\pm \nu_y} \rangle, 1.0)$  both are found to be 0.5 following the mirror rotation symmetries generated by  $\mathcal{M}_{xy}$  and  $\mathcal{M}_{x\bar{y}}$ . Moreover, under these mirror rotation symmetries, one can show that  $\nu_x^{\nu_y}(k_y) \rightarrow -\nu_x^{\nu_y}(-k_y)$  and  $\nu_y^{\nu_x}(k_x) \rightarrow -\nu_y^{\nu_x}(-k_x)$ . We further notice that when  $\mathcal{M}_{xy}$  is broken,  $\langle \nu_{y,\mu'}^{\pm \nu_x} \rangle$  and  $\langle \nu_{x,\mu'}^{\pm \nu_y} \rangle$  do not produce a quantized value of 0/0.5. Therefore, these spatial symmetries can predict the quantization of the second-order polarization that determines the second-order topology. In this regard, we would like to comment that the winding number, based on the mirror rotation symmetry  $\mathcal{M}_{xy}$  and the sublattice symmetry  $\mathcal{S}$ , is shown to topologically characterize the NH higher-order topological insulator (HOTI) [100]. We believe that it is possible to define such a winding number yielding quantized values in the SOTSC phase as our NH model preserves mirror rotation and sublattice symmetries.

Note that winding number, usually characterizing a first-order topological phase provided Hamiltonian preserves sublattice symmetry [133], can also identify a second-order topological phase while appropriately defined with other symmetry constraints. The winding number for a Hamiltonian physically means how many times the Hamiltonian encircles a given point when a parameter is cyclically varied. On the other hand, half integer eigenvalues of nested Wilson loop refers to the fact that Wannier centers, located at a high-symmetry point with respect to the mirror symmetries, lie half-way between the lattice sites for higher-order topological phase [10]. Therefore, both the above invariant captures the non-trivial nature of the underlying wave-functions in the Brillouin zone through either Wannier

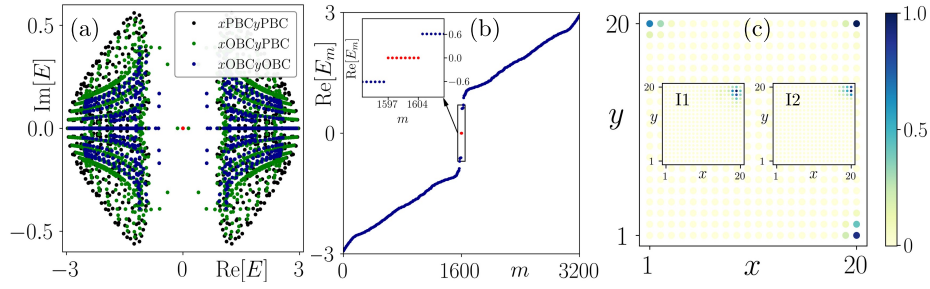


FIG. S3. (a) The eigenvalue spectrum for the real space 2D system, obeying PBC in both direction (black dots), PBC in  $y$  and OBC in  $x$ -direction (green dots), and OBC in both directions (blue dots) are depicted in complex energy plane. The zero-energy mode, obtained from OBC, is marked by red dots. (b)  $\text{Re}[E_m]$  as a function of the state index  $m$  is displayed where eight mid-gap MZMs are highlighted in the inset. (c) The LDOS, associated with eight MZMs in (b), show sharp localization only at one corner. We choose  $E_m = -2.666466$  and  $E_m = -1.713832 + 0.038500i$  for insets I1 and I2 in (c), respectively. The parameters used here are  $t_x = t_y = \lambda_x = \lambda_y = \Lambda = 1.0$  and  $\Delta_s = \gamma_x = \gamma_y = 0.4$ .

center or winding number once a certain set of symmetries is present. The winding number thus can be considered to be equivalent to our nested Wilson loop eigenvalues i.e, second-order Wannier values. The quantization in  $\langle \nu_{y,\mu'}^{\pm\nu_x} \rangle$  and  $\langle \nu_{x,\mu'}^{\pm\nu_y} \rangle$  might be intimately connected to winding number as stated above. However, the detailed mathematical proof is an open question yet, to the best of our knowledge, that we leave for future studies.

#### S4. $s$ -WAVE NH SOTSC

In the main text, we discuss  $d$ -wave proximized to engineer NH SOTSC phase. We here illustrate that NH higher-order topological superconductor (HOTSC) can be contemplated for  $s$ -wave superconductivity with pairing amplitude  $\Delta_s$  as follows [28, 63]  $\mathcal{H}(\mathbf{k}) = \mathbf{N} \cdot \mathbf{\Gamma}$ ; where,  $\mathbf{N} = \{\lambda_x \sin k_x + i\gamma_x, \lambda_y \sin k_y + i\gamma_y, m_0 - t_x \cos k_x - t_y \cos k_y, \Delta_s, \Lambda(\cos k_x - \cos k_y)\}$ ,  $\mathbf{\Gamma} = \{\tau_z \sigma_x s_z, \tau_z \sigma_y s_0, \tau_z \sigma_z s_0, \tau_x \sigma_0 s_0, \tau_0 \sigma_x s_x\}$ . The last term proportional to  $\Lambda$  represents  $C_4$  symmetry breaking Wilson-Dirac mass term. We depict the corresponding complex-energy bands in complex energy plane, eigenvalue spectra highlighting the mid-gap states, and the LDOS associated to the MZMs and bulk modes in Fig. S3 (a), (b), and (c), respectively. The NH SOTSC phase with  $\Delta_s$  can also be obtained using in-plane magnetic field instead of  $C_4$  symmetry breaking [30, 63]. The topological characterization of these phases we leave for future studies.

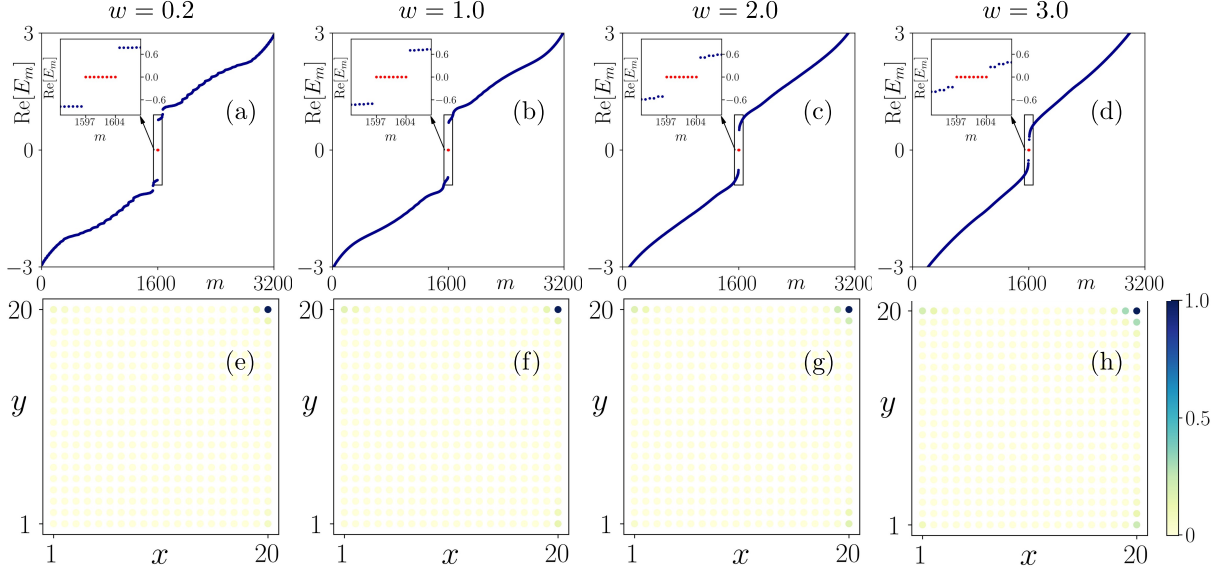


FIG. S4. We depict the eigenvalue spectra  $E_m$  and local density of states in (a), (e) for  $w = 0.2$ , (b), (f) for  $w = 1.0$ , (c), (g) for  $w = 2.0$ , and (d), (h) for  $w = 3.0$ . One see that even for a very high-disorder strength, the Majorana zero modes are robust.



## S5. EFFECT OF ONSITE DISORDER

In this section, we investigate the effect of on-site disorder to investigate the stability of the MZMs. We consider an onsite disorder potential of the form  $V(i, j) = \sum_{i,j} V_{ij} \Gamma_3$ . Here,  $V_{ij}$  is randomly distributed in the range  $V_{ij} \in [-\frac{w}{2}, \frac{w}{2}]$ ; while  $w$  accounts for the strength of the disorder potential. The disordered NH Hamiltonian  $\mathcal{H}'(i, j) = \mathcal{H}(i, j) + V(i, j) \Gamma_3$  respects the chiral symmetry while investigating the extended Hermitian Hamiltonian  $\tilde{\mathcal{H}}'$ :  $\mathcal{S} \tilde{\mathcal{H}}' \mathcal{S}^{-1} = -\tilde{\mathcal{H}}'$  with  $\mathcal{S} = \mu_0 \tau_y \sigma_0 s_0$ . We also note that on-site disorder preserves  $\mathcal{M}_{xy}$ . In the presence of the onsite disorder, the real-space Hamiltonian  $\mathcal{H}'$  is given as

$$\begin{aligned} \mathcal{H}' = & \sum_{i,j} \Psi_{i,j}^\dagger [i\gamma_x \Gamma_1 i\gamma_y \Gamma_2 + (m_0 + V_{ij}) \Gamma_3] \Psi_{i,j} + \sum_{\langle i,j \rangle_x} \Psi_{i,j}^\dagger \left[ -\frac{i\lambda_x}{2} \Gamma_1 - \frac{t_x}{2} \Gamma_3 + \frac{\Delta}{2} \Gamma_4 \right] \Psi_{i,j} \\ & + \sum_{\langle i,j \rangle_y} \Psi_{i,j}^\dagger \left[ -\frac{i\lambda_y}{2} \Gamma_2 - \frac{t_y}{2} \Gamma_3 - \frac{\Delta}{2} \Gamma_4 \right] \Psi_{i,j}. \end{aligned} \quad (\text{S2})$$

Here,  $\Psi_{i,j}$  is a  $8 \times 1$  matrix consisting of the annihilation operator in the particle-hole, orbital, and spin subspace at a lattice site  $(i, j)$ . And  $\langle i, j \rangle_x$  ( $\langle i, j \rangle_y$ ) represents the nearest neighbor hopping along  $x$  ( $y$ ) direction. We consider 500 disorder configurations and depict the eigenstates  $E_m$  as a function of the state index  $m$  and the LDOS of the MZMs in Fig. S4 for different disorder strengths. The MZMs remain localized at a given corner due to the mirror symmetry preserving nature of the on-site disorder. We can conclude from the eigenvalue spectra and the LDOS plot that the MZMs are robust and against the onsite disorder.

## S6. TUNING THE NUMBER OF MCMS DYNAMICALLY

In this section, we discuss how Floquet engineering permits us to generate more in-gap states (both 0- and  $\pi$ -gap) by tuning the different driving parameters suitably. The generation of multiple in-gap states is attributed to higher-order hoppings generated in the dynamical system. The mass-kick protocol, introduced in Eq. (9) of the main text, can be used to create multiple Majorana corner modes (MCMs). We depict the real part of the quasienergy spectra as a function of the driving frequency  $\Omega$  in Fig. S5 (a). In order to understand the generation of the MCMS more clearly, we exemplify two cases in Fig. S5 (b) and (c) for  $\Omega = 4.6$  and 1.9, respectively. In Fig. S5 (b), the number of 0-MCMs is twice that of the static case, whereas the number of  $\pi$ -MCMs remains the same. While in Fig. S5 (c), the number of  $\pi$ -MCMs is thrice compared to the case in the main text (see Fig. 4 (a) of the main text).

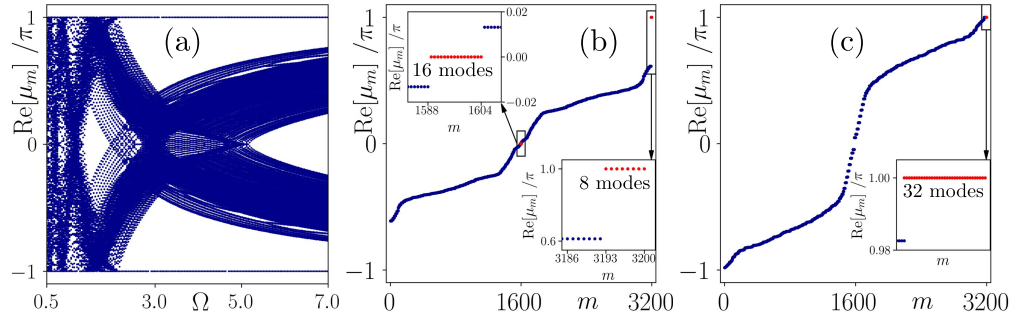


FIG. S5. We depict the real part of the quasienergy spectra  $\text{Re}[\mu_m]$  as function of the driving frequency  $\Omega$  in (a). We exhibit the quasienergy spectra as function of the state index  $m$  for two individual cases in (b) with 16 0-MCMs and 8  $\pi$ -MCMs, and (b) 32  $\pi$ -MCMs. We consider  $\Omega = 4.6$  for (b) and  $\Omega = 1.9$  for (c). While all the other parameters take the value:  $m_0 = 0.0$ ,  $m_1 = 2.5$ ,  $t_x = t_y = \lambda_x = \lambda_y = \Delta = 1.0$ , and  $\gamma_x = \gamma_y = 0.4$ .